RESEARCH ARTICLE | AUGUST 04 2023

Uncooled mid-wavelength InAsSb/AlAsSb heterojunction photodetectors

Yeongho Kim ; Saud Alotaibi ; Mohamed Henini ; Byong Sun Chun ; Sang Jun Lee

APL Mater 11, 081104 (2023)
https://doi.org/10.1063/5.0157112

Uncooled mid-wavelength InAsSb/AlAsSb heterojunction photodetectors

Cite as: APL Mater. 11, 081104 (2023); doi: 10.1063/5.0157112
Submitted: 5 May 2023 • Accepted: 10 July 2023 •
Published Online: 4 August 2023

View Online Export Citation CrossMark

Yeongho Kim,[1] Saud Alotaibi,[2,3] Mohamed Henini,[2] Byong Sun Chun,[4,a)] and Sang Jun Lee[4,5,a)]

AFFILIATIONS

[1] School of Materials Science and Engineering, Chonnam National University, Gwangju 61186, Republic of Korea
[2] School of Physics and Astronomy, University of Nottingham, Nottingham NG7 2RD, United Kingdom
[3] Physics Department, Faculty of Science and Humanities in Ad-Dawadmi, Shaqra University, Shaqra 11911, Saudi Arabia
[4] Division of Interdisciplinary Materials Measurement Institute, Korea Research Institute of Standards and Science, Daejeon 34113, Republic of Korea
[5] Department of Nano Convergence Measurement, University of Science and Technology, Daejeon 34113, Republic of Korea

[a)] **Authors to whom correspondence should be addressed:** mainue@kriss.re.kr and sjlee@kriss.re.kr

ABSTRACT

A mid-wavelength *p*–*B*–*i*–*n* infrared photodetector constituting ternary alloys of an $InAs_{0.9}Sb_{0.1}$ absorber and an $AlAs_{0.05}Sb_{0.95}$ electron barrier was demonstrated to operate at room temperature. The results of high-resolution x-ray diffraction (XRD) analysis indicate the high crystalline quality of the barriode detector structure, grown via molecular beam epitaxy, as supported by the strong XRD peak intensity of InAsSb and its corresponding defect density as low as $\sim 2.0 \times 10^8$ cm^{-2}. The dark current of the barriode detector remained diffusion-limited in the 280–300 K temperature range, and generation–recombination became dominant at 220–260 K owing to the deep-level traps in the depletion region of the absorber and near the lattice-mismatched heterointerface of AlAsSb/InAsSb. Two distinct shallow traps in the InAsSb absorber were identified through Laplace deep-level transient spectroscopy with the activation energies of E_{t1} = 20 meV and E_{t2} = 46 meV. The E_{t1} trap is associated with the hole localization states induced by the alloy disorder of InAsSb, whereas the E_{t2} trap originated from a point defect of In vacancies in InAsSb. At 300 K, the barriode detector exhibited a 90% cutoff wavelength of 5.0 *μ*m, a peak current responsivity of 0.02 A/W, and a dark current density of 1.9×10^{-3} A/cm^2 under a bias voltage of −0.3 V, providing a high specific detectivity of 8.2×10^8 cm Hz$^{1/2}$/W.

INTRODUCTION

High-sensitivity mid-wavelength infrared (MWIR) photodetectors for near-room-temperature operation have attracted significant attention to keep up with the rapidly increasing demand for various applications, including chemical sensing, greenhouse gas detection, eye-safe range finding, and thermal imaging.[1–4] MWIR spectral bands (3–5 *μ*m) with low atmospheric attenuation are much less susceptible to water absorption and atmospheric obscurants, such as dust, smoke, and fog, than short-wavelength infrared (SWIR, 1–3 *μ*m) and long-wavelength infrared (LWIR, 8–14 *μ*m) spectral bands.[3] In addition, the MWIR spectral band has a superior thermal contrast to the LWIR band, which is associated with the partial derivative of the spectral radiant exitance obtained by Planck's blackbody radiation law with respect to temperature. It also has a much lower solar background radiation than the SWIR band, leading to a high signal-to-noise ratio (SNR) in MWIR photodetectors.[4]

II–VI and III–V compound semiconductors, such as HgCdTe, PbSe, and InSb, have predominantly been used as light absorbers in MWIR photodetectors.[5,6] HgCdTe detectors have large tunable bandgaps (E_g) of 0.15–1.6 eV, obtained by varying the alloy composition. However, they typically require Stirling-cycle cryogenic or thermoelectric cooling to achieve a fast response and a high detectivity. PbSe photoconductive detectors (E_g = 0.27 eV) with CaF_2 nanostructured coatings offer a high detectivity, approaching 4.2×10^{10} cm Hz$^{1/2}$/W at room temperature.[6,7] The noise output of PbSe detectors is subject to increase as they generate a large photocurrent owing to the low exciton binding energy induced by the large bulk dielectric constant of ~23. However, the widespread use of HgCdTe and PbSe detectors is restricted because of the toxicity of heavy metals, such as Hg, Cd, and Pb, to humans and the environment.

InAsSb-based photodetectors are being actively explored as alternatives to conventional MWIR detectors owing to the peculiar electronic and optical properties of InAsSb alloys. Bulk InAsSb alloys offer widely tunable absorption edges from the MWIR to LWIR region up to ~10 μm due to a large direct-gap bowing parameter of ~0.6 eV.[8] Furthermore, the Auger recombination process in InAsSb is highly suppressed because of low Auger coefficients of the order of 10^{-27} cm^6/s at 300 K, leading to a lower dark current and a higher operating temperature.[9] MWIR $InAs_{0.91}Sb_{0.09}$ *n–B–n* detectors with unipolar barrier materials, such as $AlAs_{0.1}Sb_{0.9}$, $Al_{0.9}Ga_{0.1}As_{0.1}Sb_{0.9}$, and $In_{0.88}Al_{0.12}As_{0.8}Sb_{0.2}$, have been developed to achieve a high SNR and, in turn, a high detectivity at 300 K.[9–11] As there are no depletion regions in the InAsSb absorber of an *n–B–n* detector structure, the generation–recombination (G–R) current, via the Shockley–Read–Hall recombination centers, is reduced. Another structural advantage is that the unipolar barrier with a high conduction band offset at the absorber–barrier heterojunction eliminates the surface Fermi level pinning in the conduction band. As a result, the majority of electron carriers do not accumulate at the surface, which is desirable for decreasing the surface leakage current in an *n–B–n* detector. In addition, the valence band offset at the heterojunction is negligible through band alignment engineering, enabling the unimpeded transport of the photogenerated minority carriers of holes to the electrical contact.

In this study, we fabricated and characterized an $InAs_{0.9}Sb_{0.1}$/$AlAs_{0.05}Sb_{0.95}$ barriode detector for the MWIR region with a 90% cutoff wavelength of 5.0 μm. The thermal activation energies were extracted from temperature-dependent dark current–voltage measurements to elucidate the dominant current transport mechanism of the barriode detector. In addition, two shallow traps for holes at 20 and 46 meV above the valence band of the InAsSb absorber were detected through Laplace deep-level transient spectroscopy (DLTS). The electrical and optical performances of the barriode detector were also evaluated using radiometric measurements.

EXPERIMENTAL DETAILS

Material design and growth

An InAsSb photovoltaic photodetector was grown on a Te-doped n-type (001) GaSb substrate in a solid-source RIBER 32P molecular beam epitaxy (MBE) system equipped with As and Sb crackers. The GaSb substrate was thermally cleaned at 500 °C under Sb_2 overpressure to entirely remove the surface oxides of Ga_2O_3 and Sb_2O_3 before MBE growth. Afterward, the reflection high-energy electron diffraction pattern changed from a diffused to a long streaky pattern, indicating an atomically smooth surface morphology. A high-quality n$^+$-GaSb buffer was grown at a substrate temperature of 480 °C and a growth rate of 0.35 monolayer (ML)/s, as shown in Fig. 1(a). A *p–i–n* structure of $InAs_{0.9}Sb_{0.1}$, with a bandgap energy of $E_g \approx 0.24$ eV, was grown lattice-matched on the buffer layer at 400 °C at a growth rate of 0.4 ML/s. A 50-nm-thick $AlAs_{0.05}Sb_{0.95}$ barrier layer ($E_g \approx 2.3$ eV) was grown between the top contact layer and absorber layer at 450 °C at a growth rate of 0.5 ML/s. Hereafter, we refer to the InAsSb detector structure as the *p–B–i–n* structure, where *B* represents the AlAsSb barrier layer. Beryllium (Be) and gallium telluride (GaTe) dopants were employed for p-type and n-type doping, respectively, with a doping concentration of 2×10^{18} cm^{-3}. Figure 1(b) shows the energy band structure of the InAsSb photodetector at 300 K under an applied bias voltage of $V_b = -0.3$ V, calculated by the nextnano software.[12] The AlAsSb unipolar barrier effectively suppresses the transport of photogenerated electrons toward the p$^+$-$InAs_{0.9}Sb_{0.1}$ top contact layer because of the presence of a large conduction band offset of ~2.0 eV at the heterointerface of the absorber and barrier. Meanwhile, photogenerated holes are transported quickly to the p$^+$-$InAs_{0.9}Sb_{0.1}$ side across the barrier layer with no potential barrier height for holes.

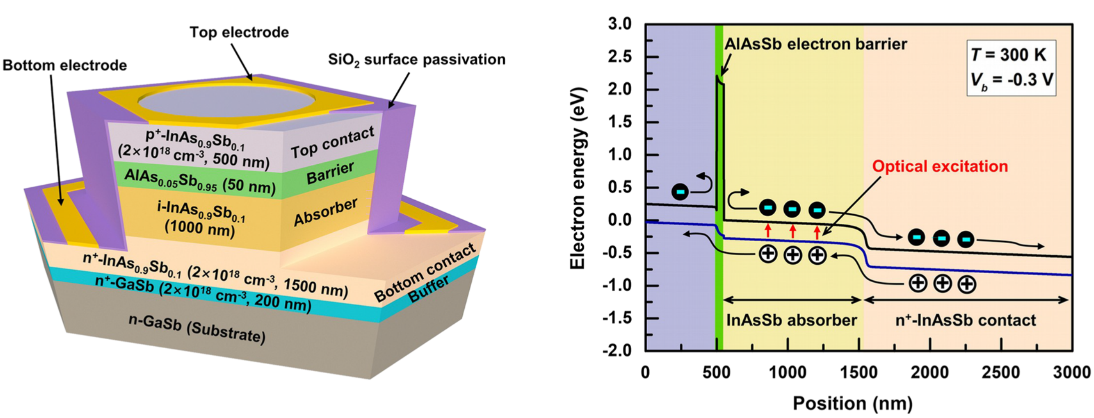

(a) (b)

FIG. 1. (a) Schematic structure of an MWIR *p–B–i–n* InAsSb/AlAsSb photodetector. (b) Calculated energy band diagram of the barriode detector under a reverse bias of −0.3 V at 300 K.

Such an efficient carrier transport and collection within the *p–B–i–n* structure is desirable for decreasing the dark current and increasing the photocurrent, resulting in a high signal-to-noise ratio of the detector.

Device processing

Conventional photolithography, etching, and metallization techniques were employed to process the as-grown epitaxial wafer into top-illuminated barriode detectors. The n^+-$InAs_{0.9}Sb_{0.1}$ bottom contact layer was etched via BCl_3-based inductively coupled plasma (ICP) etching to define the mesa area of 410 × 410 μm^2. The sidewall surface damage induced by energetic ion bombardment during ICP etching was removed using a wet etching solution of H_3PO_4:H_2O_2:H_2O (1:2:20). The surface passivation was implemented using a 200-nm-thick SiO_2 layer deposited via plasma-enhanced chemical vapor deposition. Finally, Ti (50 nm)/Ni (50 nm)/Au (300 nm) ohmic metals were deposited on both the top and bottom contact layers via electron beam evaporation, followed by rapid thermal annealing at 300 °C in an N_2 atmosphere for 30 s.

Material and device characterization

The structure of the as-grown wafer was investigated via high-resolution PANalytical x-ray diffractometry (XRD) equipped with a four-bounce Ge(220) monochromator for x-ray radiation (Cu*K*α1, λ = 1.5406 Å) and a three-bounce Ge(220) crystal analyzer. The dark current density–voltage characteristics of the InAsSb/AlAsSb barriode detector in a liquid-helium cryostat were evaluated at various temperatures of 20–300 K using a Keithley 4200-SCS semiconductor parameter analyzer. Deep-level transient spectroscopy (DLTS) was used to examine deep-level traps in the barriode detector using a 1 MHz Boonton 7200 capacitance meter with a response time of ~120 μs. Room-temperature spectral response measurements were performed on a barriode detector using a Nicolet 6700 Fourier transform infrared (FTIR) spectrometer and a Keithley 428 current amplifier. The current responsivity and specific detectivity were determined at room temperature by illuminating the barriode detector with a 900 K blackbody source modulated by an optical chopper at 400 Hz. The photocurrent and current noise density were measured using an SR850 lock-in amplifier and an SR770 fast Fourier transform network analyzer, respectively.

RESULTS AND DISCUSSION

The double-crystal XRD ω-2θ rocking curves (RCs) for single layers of 500-nm-thick $InAs_{0.9}Sb_{0.1}$ and 100-nm-thick $AlAs_{0.05}Sb_{0.95}$ are presented in Fig. 2(a). The $InAs_{0.9}Sb_{0.1}$ and $AlAs_{0.05}Sb_{0.95}$ layers were in-plane compressively strained to the GaSb substrate with in-plane lattice mismatches of 0.05% and 0.26%, respectively. Clear Pendellösung fringes on either side of the $AlAs_{0.05}Sb_{0.95}$ peak are visible, indicating that the AlAsSb/GaSb heterointerface is fairly smooth and the alloy composition is uniform across the layer. The critical thickness (h_c) of $AlAs_{0.05}Sb_{0.95}$ on GaSb for misfit dislocation formation was calculated using the mechanical equilibrium approach of Matthews and Blakeslee given by[13]

$$h_c = \frac{b}{2\pi f}\frac{\left(1-\nu\cos^2\alpha\right)}{(1+\nu)\cos\lambda}\left(\ln\frac{h_c}{b}+1\right), \quad (1)$$

where b (= 4.3 Å) is the magnitude of the Burgers vector of the misfit dislocations, f (= 2.5 × 10^{-3}) is the mismatch strain, ν (= 0.33) is the Poisson ratio of AlAsSb, α (= 60°) is the angle between the dislocation line and its Burgers vector, and λ (= 60°) is the angle between the slip direction and the direction normal to the intersection line of the slip plane and the interface. The critical thickness was determined as h_c = 288 nm, indicating that $AlAs_{0.05}Sb_{0.95}$ was pseudomorphically grown on a GaSb substrate. Figure 2(b) shows the measured and simulated ω-2θ RCs for the InAsSb/AlAsSb barriode detector, as illustrated in Fig. 1(a). The XRD intensity of the

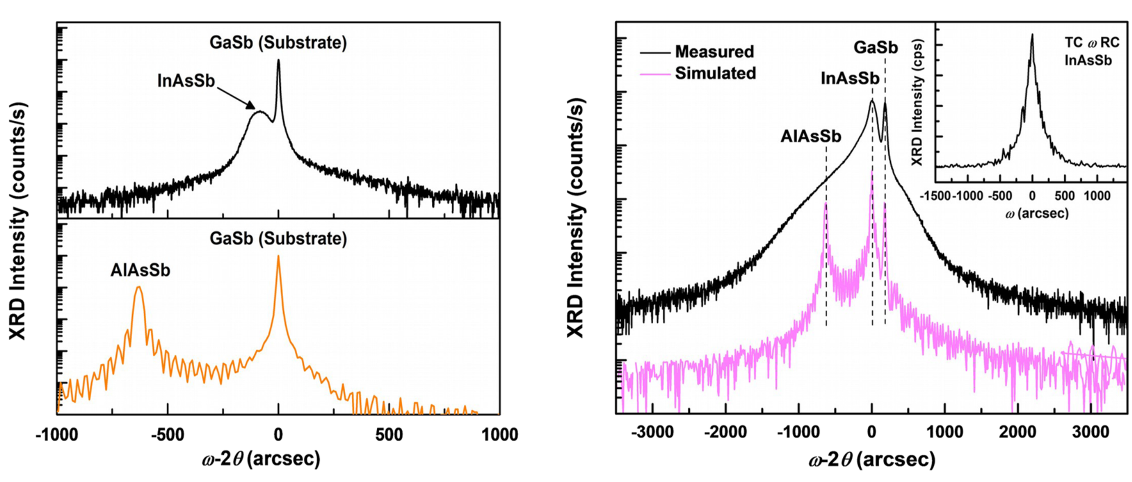

FIG. 2. (a) Measured XRD ω-2θ rocking curves of single-layered $InAs_{0.9}Sb_{0.1}$ and $AlAs_{0.05}Sb_{0.95}$ from the symmetrical (004) Bragg reflections. (b) Measured and simulated XRD ω-2θ rocking curves of the as-grown barriode detector structure. The inset shows the ω rocking curve of the $InAs_{0.9}Sb_{0.1}$ absorber measured in a triple-crystal mode.

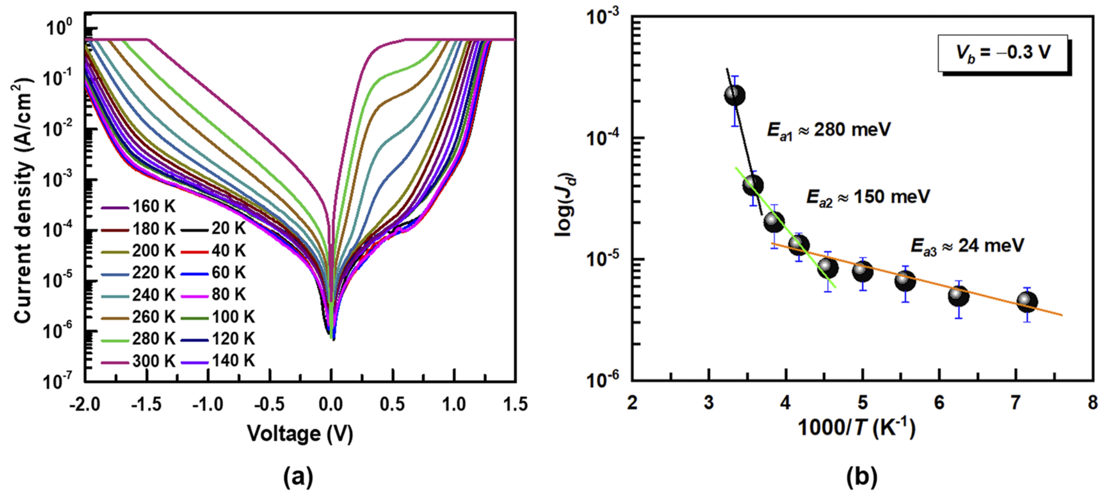

FIG. 3. (a) Dark current density–voltage characteristics of the barriode detector measured at various temperatures ranging from 20 to 300 K. (b) Arrhenius plot of the measured dark current densities in the temperature range of 140–300 K at −0.3 V.

3000-nm-thick $InAs_{0.9}Sb_{0.1}$ multilayer device structure is comparable to that of the GaSb substrate because of the increased crystalline volume with thickness. The XRD peak for the 50-nm-thick AlAsSb was not measured in the ω-2θ RC because its weak intensity was superimposed on the background of x-ray diffuse scattering of crystal imperfections in InAsSb. The inset of Fig. 2(b) displays the ω RC for InAsSb, which was established in a triple-crystal configuration to estimate the dislocation density in the volume of the layer. The full width at half maximum (FWHM) was determined as 270 arcsec for the coherent peak of the InAsSb ω RC. The dislocation density in InAsSb is linearly proportional to the square of the FWHM of the ω RC.[14] From the ω-scan, the dislocation density in InAsSb was determined as ~2.0×10^8 cm^{-2}.

Figure 3(a) depicts the dark current density–voltage characteristics of the p–B–i–n InAsSb/AlAsSb barriode detector as a function of temperature from 20 to 300 K. The dark current density of the detector was as low as 1.9×10^{-3} A/cm^2 at 300 K and $V_b = -0.3$ V. This current density is approximately two orders of magnitude lower than that of an InAsSb/$AlAs_{0.1}Sb_{0.9}$ n–B–n detector operating at the same temperature and bias voltage.[15] Our current density is four to five orders of magnitude lower than those of InSb p–n junction based detectors at 300 K.[16,17] In addition, our detector shows a 0.04 times

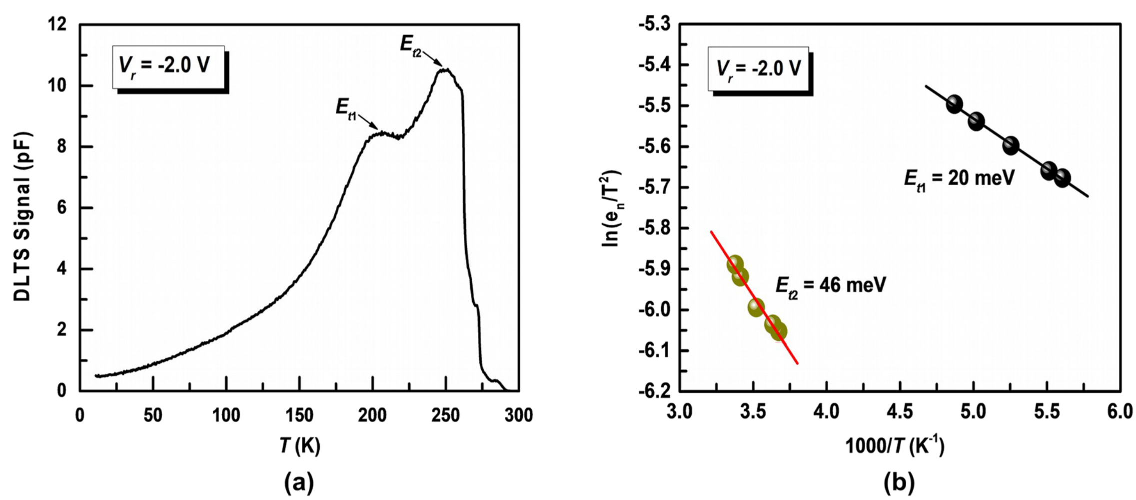

FIG. 4. (a) DLTS spectrum obtained on the barriode detector under a reverse bias of −2.0 V. (b) Arrhenius plot of the emission rate and temperature for the two shallow traps, E_{t1} and E_{t2}, detected at −2.0 V by Laplace DLTS. The trap energy levels are extracted from the linear slope of the Arrhenius plot.

lower current density at 300 K when compared to a HgCdTe detector.[18] An Arrhenius plot of the logarithmic dark current density (J_d) vs inverse temperature, as shown in Fig. 3(b), was realized to examine the dominant current mechanism in the barriode detector using the following relation:[19]

$$J_d(T) = \gamma T^{\rho} e^{-\frac{E_a}{k_B T}}, \quad (2)$$

where γT^{ρ} is the empirical fitting parameter, E_a is the thermal activation energy, and k_B is Boltzmann's constant. The activation energy for the temperature range of 280 K < T < 300 K, which is proportional to the slope of the Arrhenius plot, was calculated as $E_{a1} \approx 280$ meV. This is close to the bandgap energy ($E_g = 250$ meV) of the InAsSb absorber, as shown in Fig. 1(b), indicating that the dark current of the barriode detector is diffusion-limited in the temperature regime at $V_b = -0.3$ V. A clear transition in the slope of the Arrhenius plot can be observed in the temperature range of 220 K < T < 260 K. The activation energy for the lower temperature range was determined as $E_{a2} \approx 150$ meV, which is close to half the bandgap of the absorber. Moreover, in the temperature range of 220–260 K, the dark current of the barriode detector was dominated by the G–R of carriers in the InAsSb absorber. The G–R current was produced because of crystalline defects located near the mid-gap in the depletion region of the absorber, acting as Shockley–Read–Hall recombination centers. An additional source for the G–R current is the reduction in the G–R lifetime (τ_{GR}) near the lattice-mismatched heterointerface of AlAsSb/InAsSb ($J_d \propto \tau_{GR}^{-1}$).[20] Moreover, a small activation energy of $E_{a3} \approx 24$ meV was obtained in the temperature range of 140 K < T < 220 K, of which the origin is detailed below.

Figure 4(a) shows the conventional DLTS spectrum from the barriode detector over the temperature range of 10–300 K at the reverse voltage of $V_r = -2.0$ V. The filling pulse height, pulse duration, and emission rate window were kept constant at $V_p = 0$ V, $t_p = 1$ ms, and $e_n = 200$ s^{-1}, respectively, for all DLTS measurements. The DLTS spectrum exhibits two broad peaks at ~205 and ~250 K, labeled E_{t1} and E_{t2}, respectively, where the higher-temperature peak has a higher amplitude than the lower-temperature peak. The peak amplitude was proportional to the trap concentration in the InAsSb absorber.[21] In addition, Laplace DLTS was applied to resolve conventional DLTS signals of traps with closely spaced energy levels. Figure 4(b) shows the Arrhenius plot obtained from high-resolution Laplace DLTS at $V_r = -2.0$ V. Two shallow traps in the temperature range of 150 K < T < 300 K are apparent at $E_{t1} = 20$ meV and $E_{t2} = 46$ meV with trap densities of 2.8×10^{15} and 3.5×10^{15} cm^{-3}, respectively. The capture cross sections determined from the y-intercept of the Arrhenius plot are 6.6×10^{-23} and 8.3×10^{-23} cm^2 for E_{t1} and E_{t2}, respectively. The first shallow trap for E_{t1} possibly originated from the hole localization states formed in the InAsSb absorber. E_{t1} was close to the activation energy ($E_{a3} \approx 24$ meV) obtained from the Arrhenius plot in Fig. 3(b), as well as the activation energy of 16 meV for hopping transport of holes in the localization states of InAs/InAs$_{1-x}$Sb$_x$ type-II superlattices (T2SL).[22] Such localization states are ascribed to the alloy disorder in InAsSb, which is mainly caused by the different surface adatom mobilities of the group-V species. The second shallow trap for E_{t2} acted as a hole trap at ~46 meV above the valence band. The E_{t2} trap is attributed to a cation vacancy (V_{In}) present in the absorber.[23] An In atom displaced to an interstitial site, generating a nearby negatively charged

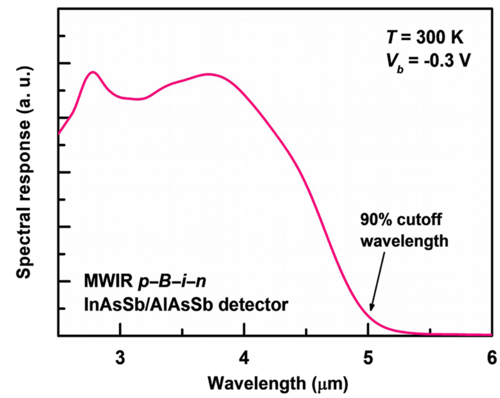

FIG. 5. Measured spectral response of the MWIR p–B–i–n InAsSb/AlAsSb barriode detector under a reverse bias of −0.3 V at 300 K, showing a 90% cutoff wavelength of 5.0 μm.

In vacancy, giving rise to a Frenkel defect (a vacancy–interstitial pair). The minority carriers of holes trapped in the E_{t2} trap can escape into the valence band edge with $E_{t2} - E_V = 46$ meV and then reach the p$^+$-InAsSb top contact layer at room temperature under an applied reverse bias because the average thermal energy of $3k_BT/2$ (≈40 meV) is comparable to the trapping potential energy.

As shown in Fig. 5, the spectral response of the barriode detector was measured at $T = 300$ K and $V_b = -0.3$ V. The peak of the spectral response is located at 2.8 μm, and the 90% cutoff wavelength is 5.0 μm. The line shape of the spectral response and the peak wavelength are associated with the interband joint density of states between the conduction and valence bands and the carrier occupation of the bands. As an important figure of merit for detector performance, the specific peak detectivity (D^*) was measured at $T = 300$ K using a calibrated radiometry system and can be expressed as[24]

$$D^* = R_p\left(2qJ_d + \frac{4k_BT}{R_dA_d}\right)^{-\frac{1}{2}}, \quad (3)$$

where R_p is the peak responsivity of the detector, q is the electron charge, R_d is the dynamic resistance determined from the dark current density curve, and A_d is the diode junction area. The peak responsivity was calculated from the measured photocurrent (I_{ph}) and the spectral photon excitation $[M_q(\lambda, T)]$ from the blackbody using the relation of $R_p \propto I_{ph}/\int M_q(\lambda, T)R(\lambda)d\lambda$, where $R(\lambda)$ is the normalized spectral response.[25] The detector responsivity was evaluated to be $R_p = 0.02$ A/W at $V_b = -0.3$ V, resulting in a specific detectivity of $D^* = 8.2 \times 10^8$ cm Hz$^{1/2}$/W. The detectivity of the p–B–i–n detector is comparable to that reported in the literature for an n–B–n detector based on an InAs/GaSb T2SL absorber ($D^* \approx 1 \times 10^9$ cm Hz$^{1/2}$/W) and an interband cascade detector with discrete InAs/GaSb T2SL absorbers ($D^* = 6.0 \times 10^8$ cm Hz$^{1/2}$/W).[26,27] Through further optimization of the crystal quality, the D^* value of our detector can be improved by more than one order of magnitude by reducing the noise current resulting from the shot noise ($2qJ_d$) and Johnson noise ($4k_BT/R_dA_d$)components.

CONCLUSION

In conclusion, we investigated the material properties and device performance of the MWIR *p–B–i–n* $InAs_{0.9}Sb_{0.1}$ barriode detector with an $AlAs_{0.05}Sb_{0.95}$ electron barrier grown via MBE. The careful design and material growth resulted in a high crystallinity of the InAsSb/AlAsSb heterostructure, as indicated by the strong peak intensity of the ω-2θ InAsSb RC comparable to that of the substrate peak and by the narrow FWHM of 270 arcsec for the ω RC, corresponding to a defect density of ~2.0×10^8 cm^{-2}. The Arrhenius plot from the temperature-dependent dark current density–voltage characteristics confirmed that the diffusion current of the barriode detector was dominant at 280–300 K. Meanwhile, the G–R current increased as the temperature was lowered to 220–260 K owing to the crystal imperfections in the absorber and near the absorber–barrier heterointerface. The Laplace DLTS experiment clearly revealed the presence of two shallow traps for minority carriers of holes located at $E_V + 20$ and $E_V + 46$ meV within the InAsSb absorber. The two traps are attributable to the hole localization states caused by the alloy disorder and the In vacancy-related point defects, respectively. The barriode detector with a 90% cutoff wavelength of 5.0 μm exhibited a dark current density of 1.9×10^{-3} A/cm^2 and a peak current responsivity of 0.02 A/W at −0.3 V, resulting in a high specific detectivity of 8.2×10^8 cm $Hz^{1/2}$/W at room temperature. The noncryogenic barriode detector demonstrates great potential for use as a detector element in MWIR focal plane array imagers, with the advantages of low cost, compact size, light weight, and low power consumption.

ACKNOWLEDGMENTS

This research was supported by the Nano·Material Technology Development Program through the National Research Foundation of Korea (NRF) funded by the Ministry of Science and ICT (Grant No. NRF-2018M3A7B4069994), the National R&D Program through the National Research Foundation of Korea (NRF) funded by the Ministry of Science and ICT (Grant Nos. 2022M3I8A2079227 and 2022M3H4A1A02076394), and the Characterization Platform for Advanced Materials funded by the Korea Research Institute of Standards and Science (Grant No. KRISS-2022-GP2022-0013).

AUTHOR DECLARATIONS

Conflict of Interest

The authors have no conflicts to disclose.

Author Contributions

Yeongho Kim: Conceptualization (equal); Data curation (equal); Formal analysis (equal); Investigation (equal); Methodology (equal); Validation (equal); Writing – original draft (equal); Writing – review & editing (equal). **Saud Alotaibi**: Data curation (equal); Formal analysis (equal); Investigation (equal); Methodology (equal). **Mohamed Henini**: Data curation (equal); Formal analysis (equal); Investigation (equal); Methodology (equal). **Byong Sun Chun**: Project administration (equal); Resources (equal); Supervision (equal). **Sang Jun Lee**: Project administration (equal); Resources (equal); Supervision (equal).

DATA AVAILABILITY

The data that support the findings of this study are available from the corresponding authors upon reasonable request.

REFERENCES

[1] J. Tong, L. Y. M. Tobing, Y. Luo, D. Zhang, and D. H. Zhang, Sci. Rep. **8**, 1548 (2018).
[2] Y. Sharabani, Y. Paltiel, A. Sher, A. Raizman, and A. Zussman, Appl. Phys. Lett. **90**, 232106 (2007).
[3] Y. Hui, S. Kang, Z. Qian, and M. Rinaldi, J. Microelectromech. Syst. **30**, 165 (2021).
[4] H. Kaushal and G. Kaddoum, IEEE Commun. Surv. Tutorials **19**, 57 (2016).
[5] P. Martyniuk and A. Rogalski, Infrared Phys. Technol. **70**, 125 (2015).
[6] M. C. Gupta, J. T. Harrison, and M. T. Islam, Mater. Adv. **2**, 3133 (2021).
[7] B. Weng, J. Qiu, Z. Yuan, P. R. Larson, G. W. Strout, and Z. Shi, Appl. Phys. Lett. **104**, 021109 (2014).
[8] I. Vurgaftman, J. R. Meyer, and L. R. Ram-Mohan, J. Appl. Phys. **89**, 5815 (2001).
[9] H. Shao, W. Li, A. Torfi, D. Moscicka, and W. I. Wang, IEEE Photonics Technol. Lett. **18**, 1756 (2006).
[10] A. Soibel, C. J. Hill, S. A. Keo, L. Hoglund, R. Rosenberg, R. Kowalczyk, A. Khoshakhlagh, A. Fisher, D. Z.-Y. Ting, and S. D. Gunapala, Appl. Phys. Lett. **105**, 023512 (2014).
[11] C. Xie, V. Pusino, A. Khalid, A. P. Craig, A. Marshall, and D. R. S. Cumming, IEEE J. Sel. Top. Quantum Electron. **24**, 7800106 (2018).
[12] See http://www.nextnano.de/nextnano3 for Nextnano[3] software.
[13] J. W. Matthews and A. E. Blakeslee, J. Cryst. Growth **27**, 118 (1974).
[14] J. E. Ayers, J. Cryst. Growth **135**, 71 (1994).
[15] E. Plis, S. Myers, M. N. Kutty, J. Mailfert, E. P. Smith, S. Johnson, and S. Krishna, Appl. Phys. Lett. **97**, 123503 (2010).
[16] K. Ueno, E. G. Camargo, T. Katsumata, H. Goto, N. Kuze, Y. Kangawa, and K. Kakimoto, Jpn. J. Appl. Phys. **52**, 092202 (2013).
[17] B. W. Jia, K. H. Tan, W. K. Loke, S. Wicaksono, and S. F. Yoon, Opt. Express **26**, 7227 (2018).
[18] W. E. Tennant, D. Lee, M. Zandian, E. Piquette, and M. Carmody, J. Electron. Mater. **37**, 1406 (2008).
[19] N. Baril, A. Brown, P. Maloney, M. Tidrow, D. Lubyshev, Y. Qui, J. M. Fastenau, A. W. K. Liu, and S. Bandara, Appl. Phys. Lett. **109**, 122104 (2016).
[20] P. C. Klipstein, Appl. Phys. Lett. **120**, 060502 (2022).
[21] H. Pettersson, C. Pryor, L. Landin, M.-E. Pistol, N. Carlsson, W. Seifert, and L. Samuelson, Phys. Rev. B **61**, 4795 (2000).
[22] B. V. Olson, J. F. Klem, E. A. Kadlec, J. K. Kim, M. D. Goldflam, S. D. Hawkins, A. Tauke-Pedretti, W. T. Coon, T. R. Fortune, and E. A. Shaner, Phys. Rev. Appl. **7**, 024016 (2017).
[23] L. Ciura, A. Kolek, E. Gomółka, K. Murawski, M. Kopytko, P. Martyniuk, and A. Rogalski, Semicond. Sci. Technol. **34**, 105017 (2019).
[24] E. Plis, J. B. Rodriguez, H. S. Kim, G. Bishop, Y. D. Sharma, L. R. Dawson, S. Krishna, S. J. Lee, C. E. Jones, and V. Gopal, Appl. Phys. Lett. **91**, 133512 (2007).
[25] D. T. Le, C. P. Morath, H. E. Norton, D. A. Cardimona, S. Raghavan, P. Rotella, S. A. Stintz, B. Fuchs, and S. Krishna, Infrared Phys. Technol. **44**, 517 (2003).
[26] J. B. Rodriguez, E. Plis, G. Bishop, Y. D. Sharma, H. Kim, L. R. Dawson, and S. Krishna, Appl. Phys. Lett. **91**, 043514 (2007).
[27] R. Q. Yang, Z. Tian, Z. Cai, J. F. Klem, M. B. Johnson, and H. C. Liu, J. Appl. Phys. **107**, 054514 (2010).